

# Photorefractive properties of ion-implanted waveguides in strontium barium niobate crystals

D. Kip<sup>1</sup>, B. Kemper<sup>1</sup>, I. Nee<sup>1</sup>, R. Pankrath<sup>1</sup>, P. Moretti<sup>2</sup>

<sup>1</sup>Universität Osnabrück, Fachbereich Physik, 49069 Osnabrück, Germany  
(Fax: +49-541/969-2670, E-mail: Detlef.Kip@Physik.uni-osnabrueck.de)

<sup>2</sup>Laboratoire de Physico-Chimie des Matériaux Luminescents, Université Claude Bernard Lyon 1, 69 622 Villeurbanne, France  
(Fax: +33-78 89 74 10, E-mail: PMoretti@dpmsun1.univ-lyon1.fr)

Received: 20 February 1997/Revised version: 1 May 1997

**Abstract.** Planar optical waveguides were formed in cerium-doped strontium barium niobate single crystals ( $\text{Sr}_{0.61}\text{Ba}_{0.39}\text{Nb}_2\text{O}_6$ , SBN61), either by proton or helium ion implantation. Proton-implanted samples show a large increase of dark conductivity that reduces or even prevents the recording of refractive index gratings. For waveguides formed by helium implantation this effect is absent, and they can be used for efficient holographic recording. Photorefractive properties of the waveguides are investigated by two-beam coupling. After implantation with 2.0 MeV  $\text{He}^+$  and doses of  $(0.5 - 5) \times 10^{15} \text{ cm}^{-2}$ , the samples have to be polarized again, because heating or charge effects at the crystals surface during the implantation process decreases or even reverses the effective electrooptic coefficients in the waveguiding layer. For reepoled samples, we find logarithmic gain coefficients of up to  $45 \text{ cm}^{-1}$  with time constants for the build-up of the purely  $\pi/2$ -shifted refractive index grating of the order of 1 ms for the blue lines of an  $\text{Ar}^+$  laser. Photoconductivity depends nonlinearly on light intensity with an exponent  $x \approx 0.55$ . With increasing implanted helium dose, both electronic and nuclear damage of the waveguiding layer grows, and the photorefractive properties of the waveguides are considerably degraded.

**PACS:** 42.80; 78.65; 81.40

Strontium barium niobate crystals ( $\text{Sr}_x\text{Ba}_{1-x}\text{Nb}_2\text{O}_6$ ,  $0.25 < x < 0.75$ , SBN) exhibit large electrooptic coefficients [1] and high photorefractive sensitivity [2]. For this reason SBN permits many applications in optical data storage and processing [3, 4], and a lot of fundamental research has been done demonstrating the excellent photorefractive properties of this material [5, 6].

Optical waveguides in this material may be used in combination with other components of integrated optics, e.g. laser diodes or optical fibers, which is of considerable importance for commercial optical systems. Possible devices are light modulators and optical switches with very low driving voltage. These devices only utilize the electrooptic properties of the crystal. In addition, the high light intensities one can reach

very easily in waveguide structures in conjunction with the good photorefractive properties enable several wave-mixing techniques like beam-coupling, phase conjugation [7, 8], or optical switching based on soliton propagation [9] to be performed.

Planar waveguide formation in SBN crystals has been performed by Bulmer and co-workers [10] using sulphur indiffusion, but the achieved waveguides exhibit high losses and small index changes. Recently, low-loss waveguides in undoped SBN have been fabricated by a refractive index increase because of the static strain-optic effect [11].

$\text{He}^+$  implantation in SBN was first mentioned by Youden et al. [12] in 1992. This technique has been successfully applied to several other ferroelectric oxide crystals, e.g.,  $\text{LiNbO}_3$ ,  $\text{KNbO}_3$  or  $\text{BaTiO}_3$  by using  $\text{He}^+$  [13–15] or  $\text{H}^+$  [12, 16] ions. In 1995, we have investigated in detail the fabrication of planar SBN61 waveguides by  $\text{H}^+$  and  $\text{He}^+$  implantation [17]. As a result, low-loss waveguides were obtained for low doses of helium implantation or intermediate doses using protons. Later, beam-coupling in cerium-doped SBN waveguides formed by  $\text{He}^+$  implantation was demonstrated by Robertson et al. [18].

In this paper we report on the investigation of the photorefractive properties of planar optical waveguides in cerium-doped  $\text{Sr}_{0.61}\text{Ba}_{0.39}\text{Nb}_2\text{O}_6$  crystals, fabricated by  $\text{H}^+$  and  $\text{He}^+$  implantation. Relative amplification, logarithmic gain coefficients, grating build-up time and photoconductivity are determined by wave-mixing experiments as a function of light intensity and wavelength and for samples with different fabrication conditions.

## 1 Theoretical description

When two coherent plane waves  $I_S$  and  $I_R$  illuminate a photorefractive crystal (e.g. SBN), propagating in the  $xz$ -plane at an angle  $\pm\theta$  with respect to the  $x$ -axis, they form an interference pattern

$$I(z) = I_0[1 + m \cos(kz)] \quad (1)$$

with the modulation  $m = 2\sqrt{I_S I_R}/I_0$ ,  $I_0 = I_S + I_R$ . Here  $k$  is the grating wavevector,  $|k| = 4\pi \sin(\theta)/\lambda = 2\pi/\Lambda$ , where  $\lambda$  is the light wavelength and  $\Lambda$  is the grating period. The  $c$ -axis of the crystal is parallel to the  $z$ -direction.

Redistribution of excited charge carriers leads to the build-up of a space charge field  $E_{sc}$  that modulates the ordinary and extraordinary refractive indices  $n_{o,e}$  via the electrooptic effect,

$$\Delta n_{o,e} = -\frac{1}{2} n_{o,e}^3 r_{13,33} E_{sc,3}. \quad (2)$$

Here  $r$  denotes the electrooptic tensor. The temporal development of the amplitude  $\Delta n^s$  of the refractive index modulation during writing and decay of the grating can be described by exponential laws [19],

$$\Delta n_{o,e}(t) = \Delta n_{o,e}^s \left[ 1 - \exp\left(-\frac{t}{\tau}\right) \right], \quad (3)$$

$$\Delta n_{o,e}(t) = \Delta n_{o,e}^s \exp\left(-\frac{t}{\tau}\right), \quad (4)$$

where  $\tau = \epsilon^{st}\epsilon^0/\sigma$  is the time constant (Maxwell time) for holographic recording, and  $\epsilon^{st}$  and  $\epsilon^0$  are static and vacuum dielectric constants. The conductivity  $\sigma$  has contributions of dark and photoconductivity,  $\sigma = \sigma_d + \sigma_0 I^x$ , where the photoconductivity depends in a two-level model [20] nonlinearly on intensity with an exponent  $0.5 \leq x \leq 1$ .

The diffraction efficiency  $\eta$  is defined as the ratio of diffracted and total transmitted light intensity. It is connected to the amplitude of the refractive index modulation and interaction length  $L$  via Kogelnik's equation,

$$\eta = \frac{I_{S'}}{I_{S'} + I_{R'}} = \sin^2\left(\frac{\pi L \Delta n}{\lambda \cos(\theta)}\right). \quad (5)$$

When the recorded refractive index grating is not in phase or antiphase with the light intensity pattern, the signal beam  $I_S$  can be amplified by the pump beam  $I_R$ . The logarithmic gain coefficient  $\Gamma$  of two-wave mixing is described by

$$\Gamma = \frac{1}{L} \ln\left(\frac{I_{S'} I_R}{I_{R'} I_S}\right) = -\frac{4\pi \Delta n_\phi}{m \lambda \cos(\theta)}. \quad (6)$$

Here  $\Delta n_\phi$  is the  $\pi/2$ -shifted part of the refractive index grating. The relative amplification  $\gamma_0$  of the signal wave can be expressed in the form

$$\gamma_0 = \frac{I_{S'}}{I_S} = \frac{(1 + \beta) \exp(\Gamma L)}{1 + \beta \exp(\Gamma L)}, \quad (7)$$

with  $\beta = I_S/I_R$  as the intensity ratio of the interacting waves.

For small interaction lengths  $L$  and comparable light intensities  $I_S \approx I_R$ , the time evolution of two-wave mixing can be expressed by a Taylor expansion of zero and first order,

$$I_{S'}(t) = I_S + \frac{I_S \Gamma L}{2} \left[ 1 - \exp\left(-\frac{t}{\tau}\right) \right]. \quad (8)$$

## 2 Experimental methods

### 2.1 Waveguide fabrication

The implantation of light ions with high energy of some MeV into oxide crystals results in the formation of a buried damaged layer of reduced refractive index compared to the substrate material [21].

A numerical TRIM (Transport and Ranges of Ions in Matter) simulation of the implantation process is given in Fig. 1 for 2.0 MeV  $\text{He}^+$  implantation into SBN61 and a dose of  $1 \times 10^{15}$  ions per  $\text{cm}^2$ . The ions lose most of their energy by electronic ionizations during their path inside the crystal and for low kinetic energy of the ions, a large number of nuclear collisions occur that can result in a significant reduction of the refractive index. Note that the refractive index decrease is related to this nuclear damage; the concentration of deposited  $\text{He}^+$  ions is of minor importance.

Our investigations were carried out using cerium-doped  $\text{Sr}_{0.61}\text{Ba}_{0.39}\text{Nb}_2\text{O}_6$  crystals with a concentration of 0.1 wt.%  $\text{CeO}_2$  in the melt. All samples have been polarized and precisely polished for endface coupling. Typical dimensions are  $2.5 \times 5.0 \times 1.0 \text{ mm}^3$ , with the 5 mm edges along the  $c$ -axis of the crystal. The samples were irradiated at room temperature with  $\text{H}^+$  ions at an energy of 1.0 MeV and doses of  $(1 - 80) \times 10^{15} \text{ cm}^{-2}$ , or  $\text{He}^+$  ions at an energy of 2.0 MeV and doses of  $(0.5 - 60) \times 10^{15} \text{ cm}^{-2}$ , respectively. During the implantation the temperature of the crystals was controlled by a combination of resistive heating and liquid nitrogen cooling, stabilizing the temperature to about  $30^\circ\text{C}$ . The irradiated face of the  $y$ -cut crystal was slightly tilted with respect to the beam axis. To reduce heating of the sample surface it is preferable to work with a relatively low ion beam flux of  $0.06 \mu\text{Acm}^{-2}$ . In Table 1, the fabrication conditions of the investigated samples are shown.

In some cases it was necessary to repolarize the crystals again after ion implantation. Sample poling is performed in two steps: First, the samples are annealed for 1 h at  $200^\circ\text{C}$  to reduce electronic and nuclear damage in the implanted layer. After this treatment, an electric field of  $700 \text{ Vmm}^{-1}$  is applied while cooling down slowly to room temperature.

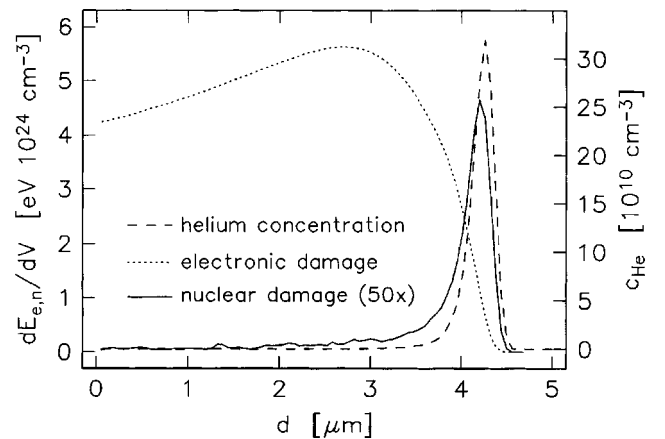


Fig. 1. TRIM simulation of implantation of 2.0 MeV  $\text{He}^+$  ions into SBN61 crystals with a total dose of  $1 \times 10^{15}$  ions per  $\text{cm}^2$ . Energy losses  $dE_e/dV$ ,  $dE_n/dV$ , and helium concentration  $c_{\text{He}}$  as a function of depth  $d$  measured from the substrate surface

**Table 1.** Fabrication parameters of the implanted planar waveguides in SBN61. E: ion energy; D: ion dose; F: beam flux

Sample	Ion	E [MeV]	D [cm <sup>-2</sup> ]	F [μAcm <sup>-2</sup> ]
SBN-H	H <sup>+</sup>	1.0	1.5 × 10 <sup>16</sup>	0.30
SBN00	He <sup>+</sup>	2.0	1.0 × 10 <sup>15</sup>	0.30
SBN3a	He <sup>+</sup>	2.0	0.5 × 10 <sup>15</sup>	0.06
SBN3b	He <sup>+</sup>	2.0	1.0 × 10 <sup>15</sup>	0.06
SBN3c	He <sup>+</sup>	2.0	2.0 × 10 <sup>15</sup>	0.06
SBN3e	He <sup>+</sup>	2.0	5.0 × 10 <sup>15</sup>	0.06

## 2.2 Measurement of conductivity

For the measurement of the conductivity during the ion implantation, some samples were prepared with electrodes. Small slits (0.4 mm wide, 0.8 mm depth) are cut parallel to two of the edges and perpendicular to the *c*-axis of the crystals. The slits are filled with silver paste, and the distance of these electrodes is 3 mm. The resistance of the crystal is monitored by a precise ohmmeter. During a measurement the ion beam has to be switched off for some seconds, and, as the resistance depends on temperature, for each measured point the sample surface has the same temperature of (0 ± 2)°C which is controlled by a thermocouple. From the resistance we can deduce directly the conductivity of the implanted layer.

## 2.3 Refractive index profiles

The waveguiding properties of the implanted samples were investigated by dark line spectroscopy. We used a well-characterized rutile prism and a precise rotary stage to measure the effective refractive indices of the waveguides. Both TE and TM modes were excited by extraordinarily and ordinarily polarized light ( $\lambda = 514.5$  nm), respectively, propagating along the *x*-direction. From the measured effective refractive indices we calculate the corresponding refractive index profiles by a least-squares fit algorithm that optimizes the parameters of an assumed analytical profile function [22].

## 2.4 Holographic setup

The experimental setup used for two-wave mixing (TWM) is shown in Fig. 2. Light of either an Ar<sup>+</sup> laser or a HeNe laser is coupled into and out of the planar waveguide by microscope lenses (magnification 20×). A cylindrical lens in front of the incoupling device ensures small beam divergence inside the waveguiding layer. In our experiments, the full angle formed by the two intersecting beams is 10.6° inside the crystal. Beam diameter (1/e<sup>2</sup> width of intensity) is 70 μm, resulting in an interaction length of the two beams of 0.4 mm. The pump beam is switched on periodically with a mechanical beam chopper. Data acquisition is performed by a digital oscilloscope.

## 3 Experimental results and discussion

### 3.1 Sample conductivity

In Fig. 3 the measurement of the conductivity of a 1.0 MeV H<sup>+</sup>-implanted layer (sample SBN-H) is illustrated. Here the

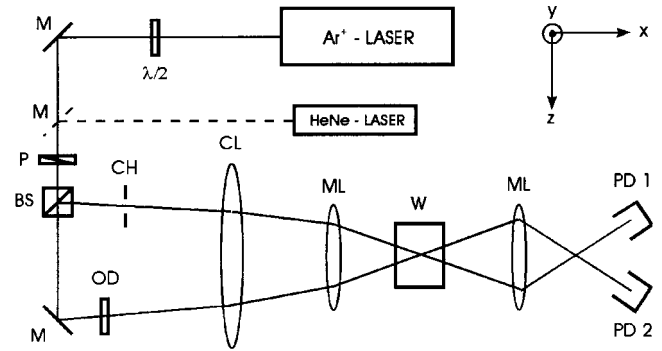


**Fig. 2.** Setup for two-wave mixing in planar SBN61 waveguides.  $\lambda/2$ :  $\lambda/2$ -plate; M: mirror; P: polarizer; BS: beamsplitter; OD: neutral density filter; CH: light chopper; CL: cylindrical lens; ML: microscope lens; W: waveguide; PD: photo detector

ion beam flux was  $0.3 \mu\text{Acm}^{-2}$ , in contrast to most other samples that have been implanted at lower flux. For the determination of the conductivity from the measured resistance, according to TRIM calculations (see Fig. 1) a conducting layer of 1 μm thickness is assumed which is comparable to the width of the implanted refractive index barrier. This assumption has been proved by slightly polishing the surface of the waveguide which gives no measurable effect on the conductivity of the sample.

As can be seen, in the case of H<sup>+</sup> implantation the conductivity of the implanted layer grows rapidly with ion dose, and we observe a temperature dependence of about  $d\sigma/dT = 10^{-3} \Omega^{-1}\text{m}^{-1}\text{K}^{-1}$ . After an implanted dose of some  $10^{15} \text{cm}^{-2}$ , the samples reach a nearly metallic conductivity. Thus necessary poling is difficult or even impossible. As has been mentioned above, the large increase of conductivity of the samples can be attributed to the damage in the implanted barrier region; the waveguiding layer itself has a much lower conductivity. In He<sup>+</sup>-implanted waveguides this effect is absent, and photorefractive properties can be investigated easily.

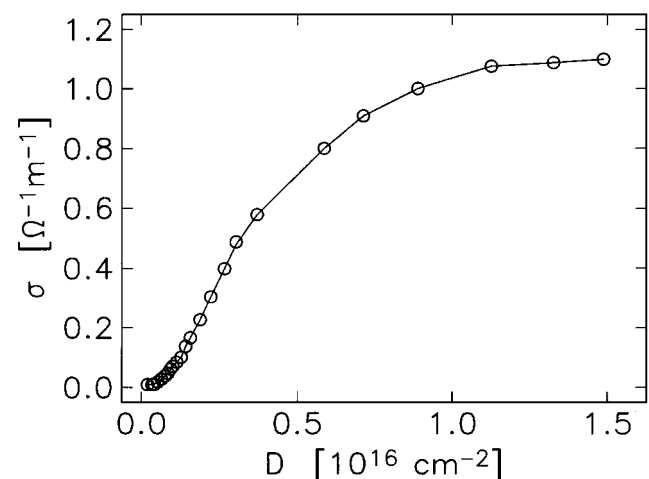


**Fig. 3.** Measurement of conductivity  $\sigma$  as a function of the implanted H<sup>+</sup> dose *D* (sample SBN-H). A conducting layer of 1 μm is assumed, and all values are measured at (0 ± 2)°C

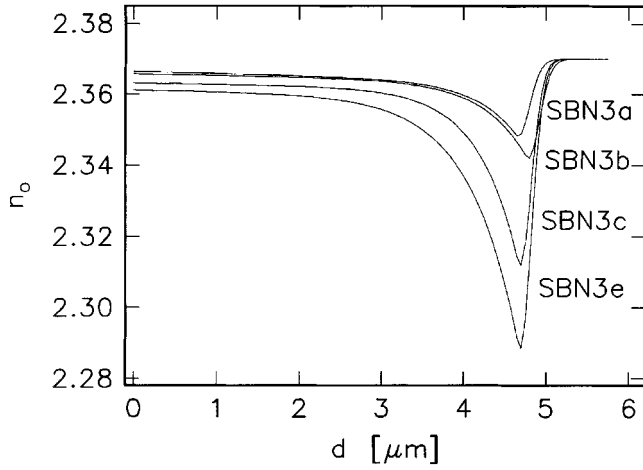


**Fig. 4.** Ordinary refractive index  $n_o$  versus depth  $d$  measured from the waveguide surface. The samples 3a-3e are implanted with 2.0 MeV  $\text{He}^+$  and doses of  $(0.5, 1, 2, \text{ and } 5) \times 10^{15} \text{ cm}^{-2}$

### 3.2 Refractive index profiles

The extraordinary refractive index profiles for the  $\text{He}^+$ -implanted samples are shown in Fig. 4. The waveguide depth is about  $4.5 \mu\text{m}$  for  $\text{He}^+$  implantation (TRIM calculation gives  $4.2 \mu\text{m}$  for the maximum of nuclear damage, see Fig. 1). For these waveguides, we observe a slight lowering of the refractive index at the surface, related to the electronic damage process that increases with the deposited ion dose. There are only very small electronic damage effects for the  $\text{H}^+$ -implanted samples.

The thermal stability of both  $\text{H}^+$ - and  $\text{He}^+$ -implanted waveguides has been investigated by isochronal annealing ( $\Delta t = 1 \text{ h}$ ) at  $T = 100\text{--}500^\circ\text{C}$ . As a result, after thermal treatment for one hour at  $300^\circ\text{C}$  more than half of the initial refractive index decrease still remains.

### 3.3 Extinction

By proton implantation we find a minimum of intensity loss of  $6.9 \text{ cm}^{-1}$  for ordinarily and a higher value of  $9.2 \text{ cm}^{-1}$  for extraordinarily polarized light at  $514.5 \text{ nm}$  and at an intermediate dose of  $4 \times 10^{16} \text{ cm}^{-2}$ . For helium-implanted waveguides both values are about  $7 \text{ cm}^{-1}$  for low doses of some  $10^{15} \text{ cm}^{-2}$ , increasing up to  $15 \text{ cm}^{-1}$  for a dose of  $6 \times 10^{16} \text{ cm}^{-2}$ .

Figure 5 illustrates the dependence of the extinction coefficients  $\alpha_{o,e}$  on the implanted  $\text{He}^+$  dose for ordinary and extraordinary polarization and a wavelength of  $514.5 \text{ nm}$ . For the investigated range of ion dose no significant changes in the extinction are observed. The losses can be attributed mainly to absorption by the substrate material itself, as the damping coefficient of the crystals used is  $\alpha_e = 6.5 \text{ cm}^{-1}$  at  $514.5 \text{ nm}$ .

### 3.4 Photorefractive properties

From the measurement of the amplified signal beam we can obtain the values of relative and logarithmic gain, and the amplitudes of shifted and total refractive index grating. From the

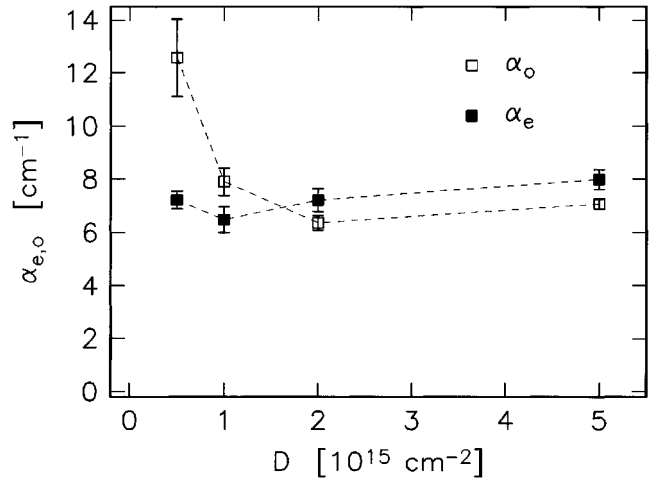


**Fig. 5.** Extinction coefficients  $\alpha_{e,o}$  of  $\text{He}^+$ -implanted samples for extraordinary and ordinary light polarization versus implanted dose  $D$ . All values are corrected for Fresnel reflections, and an efficiency of 80% for the endface coupling has been assumed. The dashed lines are merely guides for the eye

grating build-up and decay times we can calculate the values of dark and photoconductivity.

In our  $\text{He}^+$ -implanted crystals, the beam-coupling direction in the waveguiding layer is sometimes reversed compared to that in the substrate, depending on dose and ion flux. This effect has been observed for  $\text{KNbO}_3$  [7] and  $\text{BaTiO}_3$  waveguides [12], too. In our opinion, at least in our samples, this is connected with a change of the sign of spontaneous polarization due to surface heating or electric charge effects during implantation. This is not related to a change of the sign of photoexcited charge carriers, because after polarizing the samples again the beam coupling direction is the same as in the substrate.

The following results are obtained with sample SBN00. As an example, Fig. 6 presents the relative signal beam amplification  $\gamma_0$  as a function of beam intensity ratio  $\beta$  for  $\lambda = 476.5 \text{ nm}$ . From this data using (7), we can calculate the logarithmic gain coefficient  $\Gamma$ .

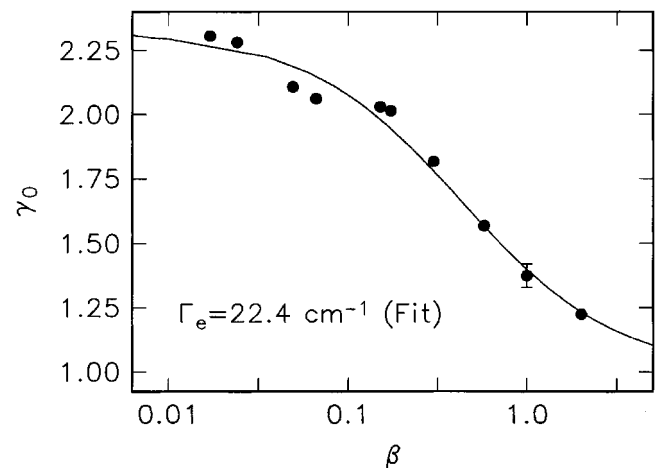


**Fig. 6.** Relative amplification  $\gamma_0$  versus signal-to-beam intensity ratio  $\beta$ , extraordinary polarization and  $\lambda = 476.5 \text{ nm}$ . The solid line is a fit according to (7), from which we obtain the logarithmic gain coefficient  $\Gamma_e = 22.4 \text{ cm}^{-2}$

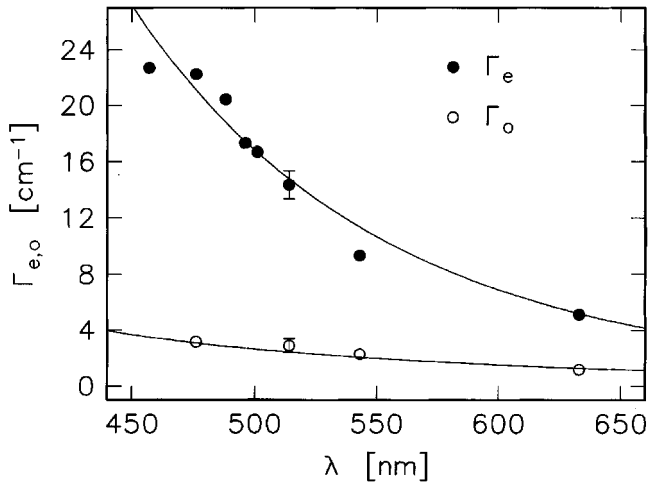


**Fig. 7.** Logarithmic gain coefficient  $\Gamma_{e,o}$  for extraordinary (●) and ordinary (○) light polarization measured for different wavelengths  $\lambda$  (sample SBN00). The dashed lines are merely guides for the eye

As can be seen in Fig. 7, the logarithmic amplification  $\Gamma$  in TWM decreases with increasing wavelength  $\lambda$ . Each measured value is the result of a fit according to (7). Maximum coefficients of  $23 \text{ cm}^{-1}$  are reached for extraordinary polarization, whereas for ordinarily polarized light all values are by a factor of 6 lower according to the smaller active electrooptic coefficient ( $r_{13}$ ,  $50 \text{ pmV}^{-1}$  instead of  $r_{33}$ ,  $280 \text{ pmV}^{-1}$ , both values for  $\lambda = 514.5 \text{ nm}$ ).

From the measurements of logarithmic gain  $\Gamma$  and that of diffraction efficiency  $\eta$  we can calculate the  $\pi/2$ -shifted part  $\Delta n_\phi \propto \Gamma$  and the total amount  $|\Delta n| \propto \sqrt{(\eta)}$  of refractive index change. The results in Fig. 8 indicate that we only have a refractive index grating shifted approximately by  $\pi/2$  relative to the intensity pattern. This shift points to diffusion as the dominant charge transport mechanism in our ion-implanted SBN61 waveguides.

For small interaction lengths and comparable light intensities of the two interacting beams, the build-up time  $\tau$  of TWM is equal to the Maxwell time. This has been proved

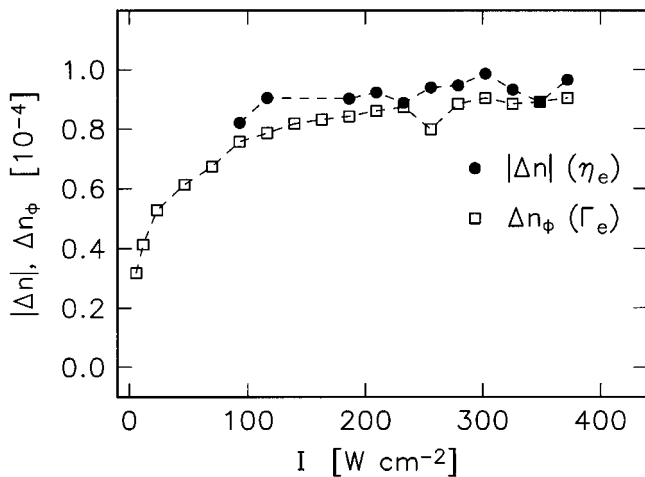


**Fig. 8.** Saturation value of total refractive index change  $|\Delta n|$  and  $\pi/2$ -shifted part  $\Delta n_\phi$  versus intensity  $I$  (sample SBN00). The data are obtained from measurements of logarithmic gain  $\Gamma$  (□) and of diffraction efficiency  $\eta$  (●) for  $\lambda = 514.5 \text{ nm}$

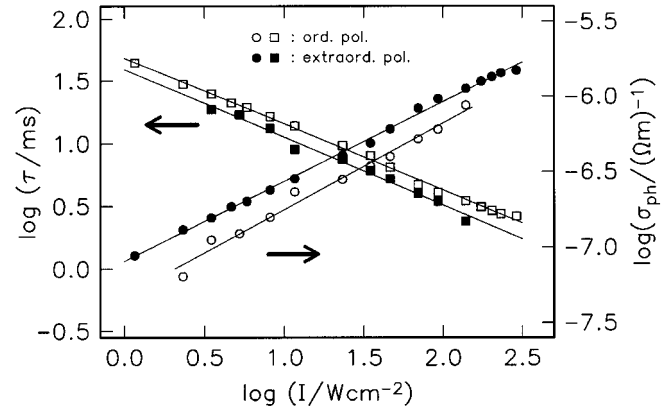


**Fig. 9.** Double logarithmic plot of grating build-up time  $\tau$  and calculated photoconductivity  $\sigma_{ph}$  versus intensity  $I$  for ordinary (○, □) and extraordinary (●, ■) polarized light (sample SBN00). The intensity ratio is 1,  $\lambda = 514.5 \text{ nm}$ , and the solid lines are linear fits to the measured values

by comparing time constants of TWM and that of erasure of the grating during read-out, when the pump beam is switched off. Thus, from measurements of the intensity dependence of  $\tau$  (Fig. 9) we can deduce dark and photoconductivity,  $\sigma_d$  and  $\sigma_{ph} = \sigma_o I^x$ .

In general, according to a two-level model for the charge transport, photoconductivity depends nonlinearly on intensity. For the  $\text{He}^+$ -implanted sample SBN00, Fig. 9 shows this sublinear photoconductivity with  $x \approx 0.55$  for both polarizations.

With increasing implanted dose, we observe a decrease of the saturation value of logarithmic gain  $\Gamma$ . Saturation is obtained at an intensity higher than  $200 \text{ Wcm}^{-2}$ . Depending on the quality of endface polishing, the values are not constant over the sample width of 5 mm, as can be seen in Fig. 10. For extraordinary light polarization a maximum amplification of about  $45 \text{ cm}^{-1}$  can be achieved for  $\lambda = 514.5 \text{ nm}$ , and for blue light these values are even slightly higher. At the same time, the grating build-up time increases from 2.2 ms (sample SBN3a) to 10.3 ms (sample SBN3e). In [17] the opposite

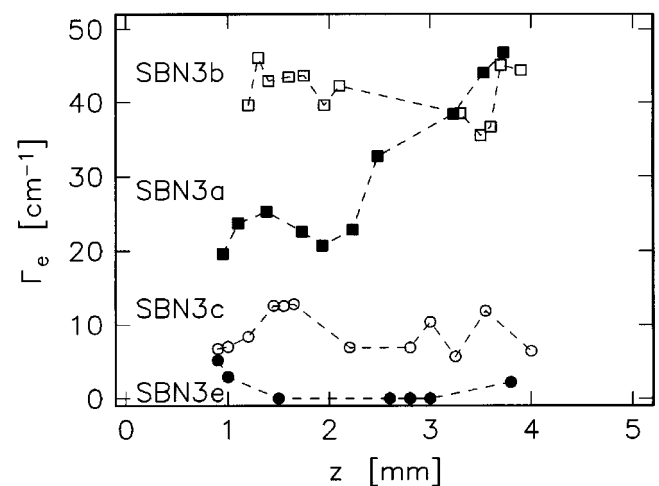


**Fig. 10.** Logarithmic gain coefficient  $\Gamma$  measured at different positions  $z$  where the light is coupled into the samples SBN3a–SBN3e. Sample width is 5 mm, and  $z = 0 \text{ mm}$  and  $z = 5 \text{ mm}$  correspond to the sample edges

effect has been found for H<sup>+</sup>-implanted samples, and was considered as a chemical reducing by the implantation. Here a different explanation may be valid because of the observed large increase of dark conductivity for H<sup>+</sup>-implanted SBN61 waveguides.

#### 4 Conclusions

In summary, planar optical waveguides in SBN61 crystals can be formed by proton and helium ion implantation. The multimode waveguides are thermally stable and have damping coefficients that are only slightly higher than those of the substrate material.

Writing of holographic gratings is possible only for He<sup>+</sup> implantation, because sample conductivity is drastically increased by the implanted H<sup>+</sup> ions. The fabricated He<sup>+</sup>-implanted waveguides, especially those with low implanted dose, exhibit interesting photorefractive properties. High logarithmic gain coefficients of two-wave mixing up to 45 cm<sup>-1</sup> together with build-up times of a few milliseconds make them interesting candidates for optical light amplification.

Further work will be concentrated on the optimization of the photorefractive properties of the samples with the aim of reducing the time for grating build-up to the order of μs. Using rhodium-doped SBN61 crystals, efficient wave mixing should be possible in the infrared, too.

*Acknowledgements.* Financial support from the Deutsche Forschungsgemeinschaft (SFB 225, D9) and the Claussen-Stiftung (TS 082/76) is gratefully acknowledged.

#### References

1. P.V. Lenzo, E.G. Spencer, A.A. Bailman: Appl. Phys. Lett. **11**, 23 (1967)
2. K. Megumi, H. Kozuka, M. Kobayashi, Y. Furuhashi: Appl. Phys. Lett. **30**, 631 (1977)
3. F. Micheron, G. Bismuth: Appl. Phys. Lett. **20**, 79 (1972)
4. P. Yeh, A.E.T. Chiou: Opt. Lett. **12**, 138 (1987)
5. M. Ewbank, R. Neurgaonkar, W. Cory, J. Feinberg: Appl. Phys. **62**, 374 (1987)
6. G.L. Wood, W. Clark III, M.J. Miller, E.J. Sharp, G.J. Salomo, R.R. Neurgaonkar: IEEE J. Quant. Electr. QE-**23**, 2126 (1987)
7. M. Zha, D. Fluck, P. Günter, M. Fleuster, C. Buchal: Opt. Lett. **18**, 577 (1993)
8. D. Kip, E. Krätzig: Opt. Lett. **17**, 1563 (1992)
9. V.M. Shandarov: Tech. Phys. Lett. **22**, 689 (1996)
10. C.H. Bulmer, O. Eknayan, H.F. Taylor, A.S. Greenblatt, L.A. Beech, R.R. Neurgaonkar: Proc. Soc. Photo-Opt. Instrum. Eng. **704**, 208 (1986)
11. J.M. Marx, Z. Tang, O. Eknayan, H.F. Taylor, R.R. Neurgaonkar: Appl. Phys. Lett. **66**, 274 (1995)
12. K.E. Youden, S.W. James, R.W. Eason, P.J. Chandler, L. Zhang, P.D. Townsend: Opt. Lett. **17**, 1509 (1992)
13. G.L. Destefanis, J.P. Gailliard, E.L. Ligeon, S. Valette, B.W. Farnery, P.D. Townsend, A. Perez: J. Appl. Phys. **50**, 7898 (1979)
14. T. Bremer, W. Heiland, B. Hellermann, P. Hertel, E. Krätzig, D. Kollwe: Ferroelectrics Lett. **9**, 11 (1988)
15. P. Moretti, P. Thevenard, G. Godefroy, R. Sommerfeld, P. Hertel, E. Krätzig: phys. stat. sol. (a) **117**, K85 (1990)
16. P. Moretti, P. Thevenard, K. Wirl, P. Hertel, H. Hesse, E. Krätzig, G. Godefroy: Ferroelectrics **128**, 13 (1992)
17. D. Kip, S. Aulkemeyer, P. Moretti: Opt. Lett. **20**, 1256 (1995)
18. E. Robertsen, R. Eason, C. Kaczmarek, P. Chandler, X. Huang: Opt. Lett. **21**, 641 (1996)
19. N.V. Kukhtarev, V.B. Markov, S.G. Odoulov, M.S. Soskin, V.L. Vinetskii: Ferroelectrics **22**, 949 (1979)
20. G.A. Brost, R.A. Motes, J.R. Rotgé: J. Opt. Soc. Am. B **5**, 1879 (1988)
21. P.D. Townsend: Nuc. Instr. and Meth. B **65**, 243 (1992)
22. P.J. Chandler, F.L. Lama: Opt. Acta. **33**, 127 (1986)